**Title**

High fidelity radiative heat transfer models for high-pressure laminar hydrogen–air diffusion flames

**Authors**

Cai, J
Lei, S
Dasgupta, A
et al.
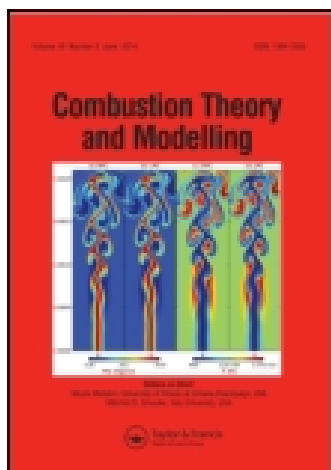
## Combustion Theory and Modelling

# High fidelity radiative heat transfer models for high-pressure laminar hydrogen–air diffusion flames

Jian Cai[a], Shenghui Lei[a], Adhiraj Dasgupta[b], Michael F. Modest[a] & Daniel C. Haworth[b]

[a] School of Engineering, University of California, Merced, CA 95343, USA

[b] Department of Mechanical and Nuclear Engineering, The Pennsylvania State University, University Park, PA 16802, USA
Published online: 02 Oct 2014.

PLEASE SCROLL DOWN FOR ARTICLE

Taylor & Francis
Taylor & Francis Group

# High fidelity radiative heat transfer models for high-pressure laminar hydrogen–air diffusion flames

Jian Cai[a], Shenghui Lei[a], Adhiraj Dasgupta[b], Michael F. Modest[a*] and Daniel C. Haworth[b]

*[a]School of Engineering, University of California, Merced, CA 95343, USA; [b]Department of Mechanical and Nuclear Engineering, The Pennsylvania State University, University Park, PA 16802, USA*

Radiative heat transfer is studied numerically for high-pressure laminar $H_2$–air jet diffusion flames, with pressure ranging from 1 to 30 bar. Water vapour is assumed to be the only radiatively participating species. Two different radiation models are employed, the first being the full spectrum $k$-distribution model together with conventional Radiative Transfer Equation (RTE) solvers. Narrowband $k$-distributions of water vapour are calculated and databased from the HITEMP 2010 database, which claims to retain accuracy up to 4000 K. The full-spectrum $k$-distributions are assembled from their narrowband counterparts to yield high accuracy with little additional computational cost. The RTE is solved using various spherical harmonics methods, such as $P_1$, simplified $P_3$ ($SP_3$) and simplified $P_5$ ($SP_5$). The resulting partial differential equations as well as other transport equations in the laminar diffusion flames are discretized with the finite-volume method in OpenFOAM®. The second radiation model is a Photon Monte Carlo (PMC) method coupled with a line-by-line spectral model. The PMC absorption coefficient database is derived from the same spectroscopy database as the $k$-distribution methods. A time blending scheme is used to reduce PMC calculations at each time step. Differential diffusion effects, which are important in laminar hydrogen flames, are also included in the scalar transport equations. It was found that the optically thin approximation over-predicts radiative heat loss at elevated pressures. Peak flame temperature is less affected by radiation because of faster chemical reactions at high pressures. Significant cooling effects are observed at downstream locations. As pressure increases, the performance of RTE models starts to deviate due to increased optical thickness. $SP_N$ models perform only marginally better than $P_1$ because $P_1$ is adequate except at very high pressure.

**Keywords:** high-pressure radiation modelling; laminar diffusion flame; spherical harmonics; full-spectrum $k$-distributions; photon Monte Carlo

## Nomenclature

### English

| | |
|---|---|
| $a$ | non-grey stretching factor [–] |
| $D$ | diffusivity [$m^2 \cdot s^{-1}$] |
| $E$ | gas emissive power [$W \cdot m^{-2}$] |
| $G$ | incident radiation [$W \cdot m^{-2}$] |
| $g$ | cumulative $k$-distribution [–] |
| $h_s$ | sensible enthalpy [$J \cdot kg^{-1}$] |
| $I$ | radiation intensity [$W \cdot m^{-2} \cdot sr$] |

---

*Corresponding author. Email: mmodest@ucmerced.edu

$I_b$  blackbody radiation intensity [$W \cdot m^{-2} \cdot sr$]
$J$  coefficient of isotropic spherical harmonics [$W \cdot m^{-2}$]
$k$  absorption coefficient variable [$cm^{-1}$]
$k^*$  correlated reordered absorption coefficient [$cm^{-1}$]
$\mathcal{L}$  Laplace transform
Le  Lewis number [–]
$\dot{m}$  mass flow rate [$kg \cdot s^{-1}$]
$\hat{\boldsymbol{n}}$  wall normal direction unit vector [–]
$n_s$  total number of species [–]
$p$  gas pressure [Pa]
$\dot{Q}$  radiative heat source [$W \cdot kg^{-1}$]
$\mathbf{q}_r$  radiative heat flux vector [$W \cdot m^{-2}$]
$R_\eta$  random number for emission wavenumber [–]
Re  Reynolds number [–]
$r$  radial coordinate [m]
$s$  radiation path length [m]
$T$  temperature [K]
$u$  gas velocity [$m \cdot s^{-1}$]
$V^c$  gas velocity correction [$m \cdot s^{-1}$]
$x$  spatial coordinate [m]
$y$  axial coordinate [m]
$Y$  species mass fraction [–]

### Greek

$\alpha$  blending factor
$\delta()$  Dirac delta function
$\delta_{ij}$  Kronecker delta [–]
$\eta$  wavenumber [$cm^{-1}$]
$\epsilon$  wall emittance [–]
$\kappa$  absorption coefficient [$cm^{-1}$]
$\kappa_P$  Planck-mean absorption coefficient [$cm^{-1}$]
$\sigma$  standard deviation in PMC
$\sigma$  Stefan–Boltzmann constant $= 5.670 \times 10^{-8}$ $W \cdot m^{-2} \cdot K^{-4}$
$\mu$  dynamic viscosity [$kg \cdot m^{-1} \cdot s^{-1}$]
$\boldsymbol{\phi}$  thermodynamic state vector
$\boldsymbol{\phi}^0$  reference thermodynamic state vector
$\tau_{ij}$  stress tensor [$kg \cdot m^{-1} \cdot s^{-2}$]
$\rho$  gas density [$kg \cdot m^{-3}$]
$\omega_\alpha$  gas species production rates of species $\alpha$ [$kg \cdot m^{-3} \cdot s^{-1}$]

### Superscript

0  reference state

### Subscript

$\alpha$  species index

## 1. Introduction

Thermal radiation makes major contributions to the heat transfer in high-pressure combustors, such as gas turbines [1,2] and rocket nozzles [3], in particular since optical thickness increases with pressure. A high-fidelity radiation model is necessary to improve numerical predictions of the overall heat transfer in such systems.

The propagation of flames at elevated pressures has been studied in laboratory facilities – see for example the references included in [4]. This includes premixed configurations such as shock tube and flow reactors, and non-premixed configurations such as laminar jet flame speed measurements and conterflow flames. The transport processes in these configurations are simplified or well controlled, so that the effects from chemical mechanisms may be separated for further study. In particular, the impact of radiative heat loss is minimized through reduced size or residence time.

On the other hand, flames in practical high-pressure applications employ non-premixed configurations. To stabilize flames in these combustors, combustion products are recirculated from downstream, and the size and residence times of combustors are increased to ensure complete mixing and reaction. These practices also increase the impact of radiative heat transfer on flames and combustor materials. For example, the optical thickness increases with enlarged size, which challenges the Optically Thin (OT) approximation radiation model commonly employed in laboratory flames [5]. The increased residence time also cools down flame in the downstream region. These issues may be addressed through high-fidelity radiation simulations, which include models with different levels of accuracy and efficiency. Therefore, one of the objectives of this study is to demonstrate qualitatively the influence of radiation on high-pressure flames. Special attention is paid to comparing the accuracy of different radiation models in flames with not-so-small optical thicknesses.

A complete description of the radiative heat transfer is given by the Radiative Transfer Equation (RTE), which includes emission, absorption and scattering of the participating media. However, the high dimensionality of RTEs prevents them from being solved exactly in general conditions. Common approximate solution methods include the spherical harmonics method, the discrete ordinates method and the statistical Monte Carlo method [6]. The Discrete Ordinates Method (DOM) is very popular in combustion solvers because of its ease of implementation and extension to high orders. However, its large computational cost results in only low order calculations in practice. The spherical harmonics method has difficulties in extending to high orders due to the complicated mathematics involved. The $P_1$ method and simplified higher order implementations, albeit their lower order truncations, are capable to provide respectable accuracy at very low computational cost. In the $P_1$ approximation, the RTE is converted into an elliptical Partial Differential Equation (PDE), which can be easily implemented within most Computational Fluid Dynamics (CFDs) solvers. Because of its low order of truncation, the $P_1$ method tends to be more accurate in media with smooth directional variation of radiative intensity [6].

The simplified $P_N$ ($SP_N$) approximation was introduced to overcome the mathematical complexity in $P_N$ approximations as a three-dimensional extension to the one-dimensional slab $P_N$-formulation [7–9]. The resulting lower order implementations, $SP_3$ and $SP_5$, are elliptic PDEs without mixed partial derivatives and contain fewer PDEs as compared to their $P_N$ counterparts. The governing equations have forms similar to that of the simple $P_1$ equation, and are coupled only through the source terms.

The Photon Monte Carlo (PMC) method, while computationally expensive, can readily be implemented for the most difficult radiative problems, such as strong spectral, spatial and directional variation of radiation properties. Its stochastic nature also makes it the

only method capable of fully evaluating Turbulence–Radiation Interaction (TRI) [5,10]. Recently, Tessé, Dupoirieux and Taine [11] implemented the PMC method to calculate radiative transfer within a sooty turbulent diffusion flame. To capture TRI, Wang, Modest, Haworth, and Wang [5,12] developed their stochastic particle-based PMC method combined with a composition Probability Density Function (PDF) method in combustion applications. The Monte Carlo method was also applied to media with non-grey absorbing–emitting– anisotropic scattering particles [13]. For radiative heat transfer in media with a variable index of refraction, a curved Monte Carlo method [14] was proposed. More recently, a two-dimensional axisymmetric finite volume PMC was developed and applied for hypersonic flow [13]. Finally, based on the superposition principle, a Monte Carlo formulation was proposed for radiative transfer in quasi-isothermal participating media [15]. Wang and Modest [16] proposed a Line-By-Line (LBL) spectral model for Monte Carlo simulations, in which the wavenumber is determined by the inversion of a random-number relation $R_\eta-\eta$. A more advanced wavenumber selection scheme has also been developed [17–19].

The spectral properties of participating media further complicate solutions of the RTE. Radiatively participating gases commonly involved in high-pressure combustion include $CO_2$, $H_2O$ and $CO$. Their absorption coefficients have strong spectral dependency. While the LBL spectral model [20,21], which resolves all spectral variations, provides the most accurate results for radiative heat transfer, its large computational demands prevent its use in practical engineering applications. Recently, full-spectrum $k$-distribution methods have been developed for gases and soot [21–23]. A $k$-distribution is a spectrally reordered absorption coefficient over a narrow-band or the full spectrum. The $k$-distribution methods reduce the computational time to a small fraction of that using LBL spectral models while retaining excellent accuracy.

Among all fuels, hydrogen has the unique advantage of zero $CO_2$ emission. However, little attention has been paid to numerical simulations of laminar hydrogen jet diffusion flames. Notable recent publications with comparisons between simulation and experiment are [24,25] and the references therein. The effects of differential diffusion due to diffusivity variation across species were confirmed by comparing experimental and numerical results in all of the studies. All studies were carried out at atmospheric pressure and radiative heat transfer was neglected or modelled by the OT approximation. Such radiation models are challenged at elevated pressures when optical thickness is increased. No modelling attempts appear to have been made of laminar hydrogen–air jet flames at high pressures.

In this study, a laminar combustion solver with differential diffusion was implemented within OpenFOAM®. Two radiative heat transfer models are considered for the combustion gases, namely PMC coupled with the LBL spectral model, and the Full-Spectrum Correlated-$k$ distribution (FSCK) spectral model coupled with a $P_1$ or $SP_N$ RTE solver. Water vapour is assumed to be the only radiatively participating gas species. Owing to the nature of the radiation, the PMC model employed in this study determines the exact radiative heat sources to the gases with negligible statistical fluctuations when coupled with the LBL spectral model [16] (i.e., only limited to the accuracy of the HITEMP spectroscopy database [26]). It is used as a reference when analytical solutions of radiation are difficult to find in a generic scenario. It was found to be very useful in modelling radiative heat transfer from flames because strong variations of flow variables and properties cause analytical solutions to be difficult, if not completely impossible, to find. When this radiative heat source is fed back into the flow energy equations, the differences between with and without radiation feedback present the radiative effects. However, the PMC model incurs high computational expense, which prompts the pursuit of low cost approximate solution models.

## 2.  Theoretical models

### 2.1.  *Laminar flame solver*

The conservation of mass for laminar flow is given by

$$\frac{\partial \rho}{\partial t} + \frac{\partial(\rho u_i)}{\partial x_i} = 0, \tag{1}$$

where $\rho$ and $u_i$ are density and velocity, respectively. The species mass fraction equation of species $\alpha$ is

$$\frac{\partial(\rho Y_\alpha)}{\partial t} + \frac{\partial(\rho u_i Y_\alpha)}{\partial x_i} + \frac{\partial(\rho V_i^c Y_\alpha)}{\partial x_i} = \dot{\omega}_\alpha + \frac{\partial}{\partial x_i}\left(\rho D_\alpha \frac{\partial Y_\alpha}{\partial x_i}\right), \tag{2}$$

where $Y_\alpha$, $\dot{\omega}_\alpha$ and $D_\alpha$ are the mass fraction, rate of production and diffusivity of species $\alpha$, respectively. Repeated $\alpha$'s are not summed. In this equation

$$V_i^c = \sum_{\alpha=1}^{N_s} D_\alpha \frac{\partial Y_\alpha}{\partial x_i} \tag{3}$$

is a correction velocity to ensure correct mass conservation. The momentum equation reads

$$\frac{\partial(\rho u_i)}{\partial t} + \frac{\partial(\rho u_i u_j)}{\partial x_j} = \frac{\partial \tau_{ij}}{\partial x_j} + \rho g_i, \tag{4}$$

where $\tau_{ij}$ is the stress tensor given by

$$\tau_{ij} = -p\delta_{ij} + \mu\left(\frac{\partial u_i}{\partial x_j} + \frac{\partial u_j}{\partial x_i}\right) - \frac{2}{3}\mu \frac{\partial u_m}{\partial x_m}\delta_{ij}, \tag{5}$$

where $\mu$ is the dynamic viscosity, and $g_i$ the gravitational acceleration. The energy equation for sensible enthalpy $h_s$ may be stated as

$$\frac{\partial(\rho h_s)}{\partial t} + \frac{\partial(\rho u_i h_s)}{\partial x_i} + \frac{\partial(\rho V_i^c h_s)}{\partial x_i} = \frac{Dp}{Dt} - \sum_{\alpha=1}^{N_s} \dot{\omega}_\alpha h_{c,\alpha} + \frac{\partial}{\partial x_i}\left(\rho D_T \frac{\partial h_s}{\partial x_i}\right)$$

$$+ \frac{\partial}{\partial x_i}\left[\rho D_T \sum_{\alpha=1}^{N_s}\left(\frac{1}{\text{Le}_\alpha} - 1\right)h_{s,\alpha}\frac{\partial Y_\alpha}{\partial x_i}\right] + \dot{Q} \tag{6}$$

where $h_{s,\alpha}$ and $\text{Le}_\alpha$ are the enthalpy of formation and Lewis number of species $\alpha$, respectively; $D_T$ the thermal diffusivity and $\dot{Q}$ is the radiative heat source.

The transport properties are evaluated by methods discussed in [27]. The species viscosity, conductivity and binary diffusivity for each pair of species are calculated first and then the mixture properties are evaluated using mixing rules. The collisional integrals involved are computed using curve fits [28]. The gases are assumed to be ideal gases.

The detailed chemistry mechanism of hydrogen oxidation reported in [4] is adopted in this study. The mechanism includes 9 species and 19 reactions. It has been validated against experimental measurements with pressures up to 100 atm. To compute the chemical

source terms in species and energy equations, the Ordinary Differential Equation (ODE) solver CVODE [29,30] from the SunDIALS package was used. CVODE is able to solve both stiff and non-stiff ODE systems. The user can choose between functional iteration (for non-stiff problems) or Newton iteration (for stiff problems). It should be noted that the purpose of this study is not to resolve flame under high pressure quantitatively, but to demonstrate the cooling effects of radiation to high-pressure laminar flames with moderate residence time. For radiation modelling purposes, only the quantitative prediction of water vapour and temperature is crucial. These variables are well predicted by most mechanisms in a flame away from its ignition point because of close to chemical equilibrium. The use of a detailed mechanism was found to stabilize numerical simulation in the time-marching to steady state scheme used in this study.

### 2.2. *Full-spectrum k-distribution method for P$_1$ and SP$_N$ RTE solvers*

The RTE for radiative intensity $I_\eta$ at wavenumber $\eta$, including absorption and emission but neglecting scattering, for participating gases is

$$\frac{dI_\eta}{ds} = \kappa_\eta I_{b\eta}(T) - \kappa_\eta I_\eta, \tag{7}$$

where $\kappa_\eta$ and $I_{b\eta}$ are the absorption coefficient and the Planck function, respectively. For non-grey gas species, the radiative heat source can be calculated using the Full-Spectrum Correlated-$k$ distribution(FSCK) method [31]. In the FSCK, the spectral variable, such as wavenumber or wavelength, is reordered by the absorption coefficient of the mixture. The resulting full-spectrum $k$-distribution is

$$f(k; \boldsymbol{\phi}^0) = \frac{1}{I_b(T)} \int_0^\infty I_{b\eta}(T)\delta(k - \kappa_\eta^0(\boldsymbol{\phi}^0)) \, d\eta, \tag{8}$$

where $\boldsymbol{\phi}^0$ is a reference state [31]. Using the cumulative $k$-distribution as a reordered spectral variable $g(k) = \int_0^k f(k) \, dk$, the spectral RTE can be restated as

$$\frac{dI_g}{ds} = k_g^* a_g I_b(T) - k_g^* I_g, \tag{9}$$

where $k_g^*$ is a correlated absorption coefficient and can be determined from the correlation assumption [31], and $a_g$ is a stretch factor [31]. The correlation assumption [31] is used here to separate the dependency on thermodynamic variables and spectral variables. If this assumption is valid, the set of spectral locations (e.g., wavenumbers) that have the same absorption coefficient value at the reference state should have equal absorption coefficient value at any other thermodynamic state. The corresponding new value is different from the absorption coefficient value at the reference state due to the change of thermodynamic states (e.g., pressure, temperature and species concentrations). The correlated absorption coefficient ($k_g^*$) reflects the variations of thermodynamic states.

In this study, water vapour is considered as the only radiatively participating species. Its full-spectrum $k$-distributions are compiled from the narrowband counterparts, with narrowband $k$-distributions databased from the HITEMP-2010 spectroscopy database [26] using the method in [32] for a wide range of temperatures and pressures.

The reordered RTE can be solved approximately with spherical harmonics methods. The simplest spherical harmonics system is the $P_1$ method. In the $P_1$ approximation, the incident radiation $G$ satisfies an elliptical PDE

$$\frac{1}{k_g^*} \nabla \left( \frac{1}{k_g^*} \nabla G_g \right) = 4\pi a_g I_b - G_g \tag{10}$$

subject to the boundary condition

$$\frac{2-\epsilon}{\epsilon} \frac{2}{3k_g^*} \hat{\boldsymbol{n}} \cdot \nabla G_g + G_g = 4\pi a_{wg} I_{bw}, \tag{11}$$

where $\epsilon$ is the wall emittance, $\boldsymbol{n}$ the wall normal direction unit vector pointing from medium to wall, $I_{bw}$ the black body emission of the wall, and $a_{wg}$ the non-grey stretching factor at the wall.

In the Simplified $P_5$ ($SP_5$) approximation [9], Equation (9) is solved approximately by three elliptical equations, which are coupled only through the source terms,

$$\frac{1}{3k_g^*} \nabla \left( \frac{1}{k_g^*} \nabla J_{0g} \right) = J_{0g} - \frac{2}{3} J_{2g} + \frac{8}{15} J_{4g} - a_g I_b \tag{12a}$$

$$\frac{3}{7k_g^*} \nabla \left( \frac{1}{k_g^*} \nabla J_{2g} \right) = -2(J_{0g} - a_g I_b) + 3 J_{2g} - \frac{12}{5} J_{4g} \tag{12b}$$

$$\frac{5}{11k_g^*} \nabla \left( \frac{1}{k_g^*} \nabla J_{4g} \right) = \frac{8}{3}(J_{0g} - a_g I_b) - 4 J_{2g} + 5 J_{4g} \tag{12c}$$

subject to boundary conditions

$$-\frac{1}{3k_g^*} \hat{\boldsymbol{n}} \nabla J_{0g} = \frac{1}{2}(J_{0g} - J_{wg}/\pi) - \frac{1}{8} J_{2g} + \frac{1}{16} J_{4g} \tag{13a}$$

$$-\frac{1}{7k_g^*} \hat{\boldsymbol{n}} \nabla J_{2g} = -\frac{1}{8}(J_{0g} - J_{wg}/\pi) + \frac{7}{24} J_{2g} - \frac{41}{384} J_{4g} \tag{13b}$$

$$-\frac{1}{11k_g^*} \hat{\boldsymbol{n}} \nabla J_{4g} = \frac{1}{16}(J_{0g} - J_{wg}/\pi) - \frac{41}{384} J_{2g} + \frac{407}{1920} J_{4g}, \tag{13c}$$

where $J_{wg} = \pi a_{wg} I_w$ is the radiosity at the wall [6]. Note that all equations were simplified for non-scattering media. The solutions of $J_{0g}$ and $J_{2g}$ are related to incident radiation by

$$G_g = 4\pi \left( J_{0g} - \frac{2}{3} J_{2g} + \frac{8}{15} J_{4g} \right). \tag{14}$$

$SP_3$ is contained within $SP_5$ by leaving out the last equation and boundary condition, and setting $J_{4g} = 0$.

For all cases, the radiative heat source is calculated from

$$\dot{Q} = -\nabla \cdot \mathbf{q}_r = \int_{g=0}^{1} k_g^* G_g \, dg - 4\pi \kappa_P I_b, \tag{15}$$

which is fed back into energy Equation (6). The integration over reordered spectral variable *g* is performed using Gaussian quadratures [22]; in this study, eight quadrature points are used.

### 2.3. *PMC-LBL radiation solver*

To calculate the part of $\dot{Q}$ in Equation (6) due to radiative heat transfer, a finite volume-based PMC method was also developed. The emitted energy comes from every cell and is divided into a limited number of photon bundles, which are released into random directions and traced until they are completely absorbed within a certain cell in the medium or escape from the domain, as discussed in [6,10]. The interaction between photon bundles and cells (i.e., absorption) is evaluated commensurate with the optical thickness that a photon bundle travels through a cell. Thus, the local radiative heat source of a cell may be calculated by the balance between the energy emitted and absorbed by a cell.

The RTE solved by PMC provides the divergence of radiative flux $\nabla \cdot \mathbf{q}_r$, for each cell, which is included as a source term in the energy equation within the laminar-diffusion solver. Since the PMC is statistical in nature, it can yield a slightly different solution for each time step. This variation may be minimized by tracing a large number of rays, but the computation would be prohibitively expensive. Instead, for statistically steady problems, tempered averaging may be used, i.e., an updated source is evaluated from

$$\nabla \cdot \mathbf{q}_r^n = \alpha \nabla \cdot \mathbf{q}_r^* + (1-\alpha)\nabla \cdot \mathbf{q}_r^{n-1}, \tag{16}$$

where $\alpha$ is a blending coefficient with a relatively small value, the superscript *n* denotes the current time step, $n-1$ represents the previous time step, and $\nabla \cdot \mathbf{q}_r^*$ is the source calculated at time step *n* using relatively few photon bundles. At each time step, the updating algorithm proposed by West [33] is used to calculate the new mean and variance of $\nabla \cdot \mathbf{q}_r$. Equation (16) reveals that the radiation solution includes information from previous tracing steps and, as a result, it does not significantly vary between time steps. In addition, it also ensures that the contribution of previous time steps gradually fades out and the radiation field can 'keep up' with the flowfield.

Ten different samples are determined and kept at every time step to allow evaluation of a standard deviation. The standard error for a tempered average [34] is calculated from

$$\mathrm{SE}_{\bar{x}} = \sigma \left[\frac{\alpha}{2-\alpha}\right]^{1/2}, \tag{17}$$

where $\sigma$ indicates the standard deviation based on $\nabla \cdot \mathbf{q}_r^*$, i.e., photons traced at time step *n*. Equation (17) shows that the solution variation will reach a constant value as the radiation field reaches a quasi-steady state.

In the PMC-LBL scheme employed in the present study, first a random number for emission wavenumber, $R_\eta$, is drawn and the emitting species *s* is determined by [19]:

$$s = j, \quad \text{if} \quad \left(\sum_{i=1}^{j-1} E_i\right) \bigg/ \left(\sum_{i=1}^{n_s} E_i\right) < R_\eta \leqslant \left(\sum_{i=1}^{j} E_i\right) \bigg/ \left(\sum_{i=1}^{n_s} E_i\right). \tag{18}$$
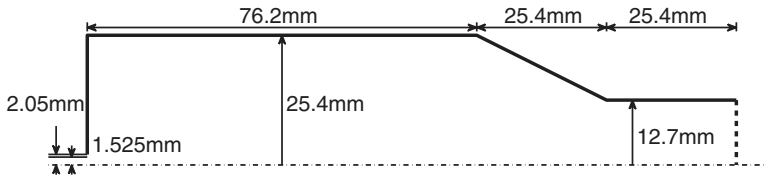
Figure 1.   Combustion chamber geometry.

Once the emitting species $s$ is determined, the emission wavenumber can be found from the tablulated $\eta - R_{\eta,s}$ database directly/by linear interpolation, which has the form

$$\eta = f_{\eta,i}(R_{\eta,i}, T, x_i), \quad \kappa_{\eta,i} = f_{\kappa,i}(\eta, T, x_i) \quad i = 1, 2, ..., n_s, \tag{19}$$

where $\kappa_{\eta,i}$ is the spectral absorption coefficient of species $i$. As discussed in [19], the $\eta - R_{\eta,s}$ database is tabulated for 28 temperatures (ranging from 300 to 3000 K) and a few mole fractions (two for $H_2O$ and one for $CO_2$ and CO). The PMC results using the new scheme [19] completely agree with the ones using the old scheme [16] and the computation costs for both schemes are nearly the same in this study because only a single species, $H_2O$, is present. With an increasing number of species, however, the new wavenumber selection displays a significant improvement in computational efficiency.

To calculate the divergence of the radiative flux, $\nabla \cdot \mathbf{q}_r$, at any given time step, about 10,000 photon bundles each are traced for ten different samples to obtain its statistical mean and standard error, which are fed back to the laminar diffusion solver in OpenFOAM®. The blending coefficient in Equation (16) is set to 0.01 during the first 1000 time steps, then to 0.001 until the 10,000th time step, and beyond that $\alpha = 0.0001$ is used to include the impact of more histories in the average when the solution is statistically converged.

### 2.4.  *Implementation*

The above models are incorporated into OpenFOAM® [35]. The solver structure is similar to OpenFOAM®'s built-in combustion solver 'reactingFoam'. The continuity, momentum, species mass fraction and energy equations are solved sequentially in a segregated manner, and pressure–velocity coupling is ensured by using the PISO algorithm as the solution is advanced in time.

The modelled chamber is axisymmetric and shown in Figure 1. The chamber has a radius of 25.4 mm with an exit of radius of 12.7 mm. The geometry is an axisymmetric approximation of the high-pressure hydrogen combustion test facility EC-1 at Edwards Air Force Base, which has a square cross section. The temperature and species concentration profiles can be measured at the exit of the chamber for comparison. The central jet has a diameter of 3.05 mm, the annular jet has an inner diameter of 4.1 mm. The wall thickness of the inner jet is neglected. The outer jet is flush with the chamber walls; therefore its thickness is part of the chamber walls. The simulation domain covers the chamber without nozzle pipe. Uniform inlet velocity and scalar profiles are applied at the nozzle exit as boundary conditions for the simulation chamber. The central jet supplies air with a temperature of 300 K and a mass flow rate of 0.143 g/s. The annulus jet supplies hydrogen with a temperature of 300 K and a mass flow rate of $4.16 \times 10^{-3}$ g/s. Simulations were performed for three pressures, viz. 1, 5 and 30 bar. In all three cases, the same mass flow rates are used. At 1 bar total pressure, the central and annulus velocities are 16.79 and
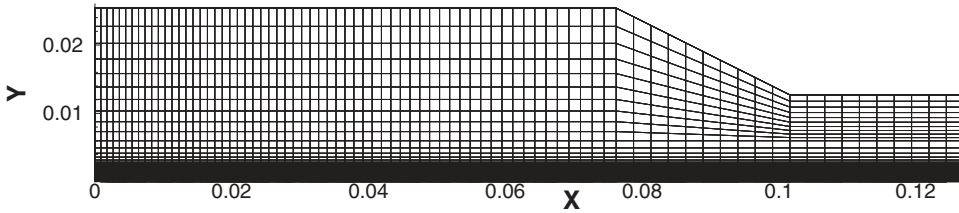
Figure 2.　Grid information.

9 m/s, respectively. The velocity is scaled with the inverse of total pressure in cases with elevated pressures. Because gas dynamic viscosity has little dependency on pressure, the Reynolds number based on air mass flow rate, viscosity and inner jet diameter is

$$\text{Re} = \frac{4\dot{m}}{\pi D \mu} = 3268 \tag{20}$$

for all pressures. This Reynolds number is much lower than the transient Reynolds number of laboratory jet flames, such as Sandia Flames [36], and is expected to result in a laminar flame.

A non-slip boundary condition is applied to all chamber walls. The wall and nozzle temperature is assumed to be 400 K, i.e., wall temperature rise and convective preheating to inlet gas due to flame radiation are not considered. This choice is due to the fact that, as the target experimental burner controls wall temperature, the experiments stop before the wall temperature reaches 800 K. However, the wall temperature used in this study has little effect on flame temperature predictions, due to low convective heat transfer at low Reynolds numbers. The radiative interaction between the wall and the gas is modelled through Marshak radiation boundary conditions. The target experimental chamber is built of pure copper. The surface is covered by copper oxide. Assuming a slightly oxidized surface, a grey wall emittance of 0.7 is used, corresponding to a wall reflectance of 0.3. Because gas radiation is highly non-grey, most of the flame emission is self-absorbed by the ambient combustion products in the chamber.

A two-dimensional cylindrical grid with 8320 cells is used to discretize all model equations, as shown in Figure 2. Most of the grid cells are placed near the flame front. Grid dependency is studied for the case of 30 bar without radiation, because it has the sharpest flame front among all cases in the study. Inclusion of radiation and/or a reduction of pressure broadens the flame front. Grid independence is confirmed through refining the mesh. It was found that, after further refining the current mesh, the temperature and mass fractions of major species ($H_2$, $O_2$, $N_2$ and $H_2O$) differ by less than 1%. The mass fractions of all minor species vary by less than 5% except that $H_2O_2$ changes by 13%. This mesh is considered sufficient for radiation simulations since flame radiation is only affected by the temperature and $H_2O$ concentration in this study.

## 3.　Results and discussion

### 3.1.　*Flow patterns*

The contour of velocity magnitude and streamlines are shown in Figure 3. Most of the streamlines close to the chamber centreline (e.g., $Y < 0.005$ m) are parallel to each other.
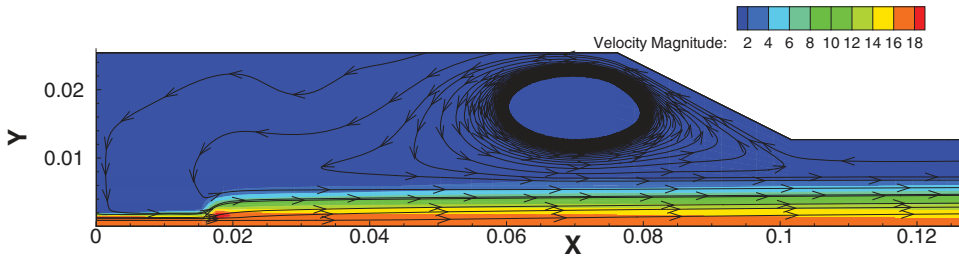
Figure 3.    Velocity magnitude (m/s) and streamlines.

Flow in this region also has a larger velocity. Because of limited viscosity in laminar flows, velocity drops quickly in the radial ($Y$) direction. Away from the centreline (e.g., $Y > 0.005$ m), velocity magnitude is small. A recirculation zone is formed at the contracting section of the chamber indicated by the circles of streamlines. Some recirculation streamlines extend to the upstream corner.



Figure 4.    Radial profiles at 1 bar. (a) Radial profiles of temperature (solid line) and $H_2O$ mass fraction (dashed line) at $x = 2.5$ cm (line with bullets), 6 cm (line with squares) and 12 cm (line with circles). Radiative flux divergence ($\nabla \cdot q$) at $x = 2.5$ cm (b), 6 cm (c) and 12 cm (d) from the nozzle.
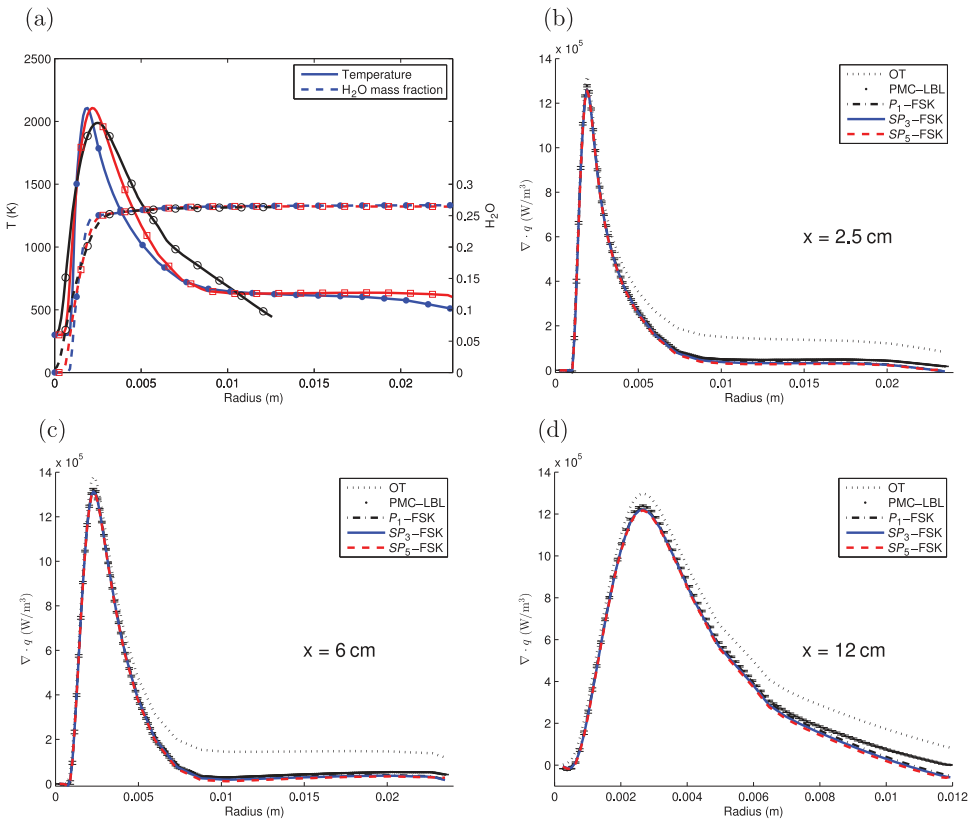
Figure 5.    Radial profiles at 5 bar. (a) Radial profiles of temperature (solid line) and $H_2O$ mass fraction (dashed line) at $x = 2.5$ cm (line with bullets), 6 cm (line with squares) and 12 cm (line with circles). Radiative flux divergence ($\nabla \cdot q$) at $x = 2.5$ cm (b), 6 cm (c) and 12 cm (d) from the nozzle (colour online).
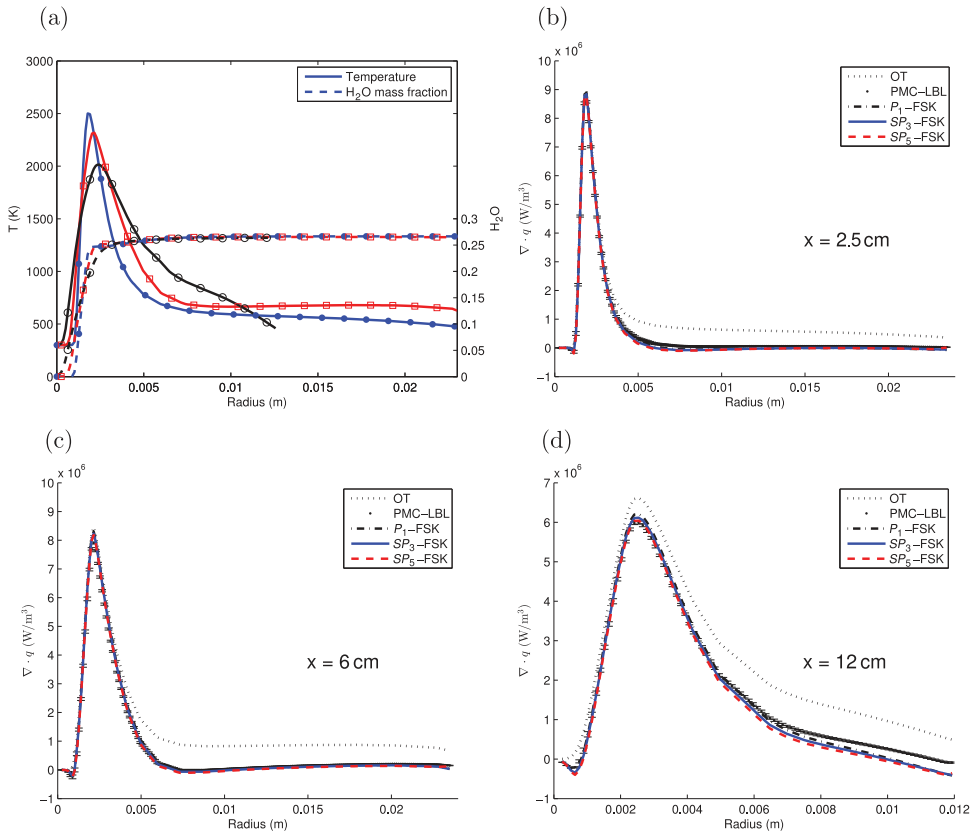
## 3.2.    *Radiative heat source calculations*

The differences between different spectral and RTE models in predicting radiative heat sources (absorption minus emission) based on scalar profiles from the fully converged PMC calculations are demonstrated in Figures 4, 5 and 6.

   The radial heat flux divergence (emission minus absorption) profiles predicted are shown at three downstream locations, namely 2.5, 6 and 12 cm from the nozzle. Two models are chosen as reference models. The OT approximation gives the total emission with absorption neglected. The OT approximation is only valid when the optical thickness is much less than unity in an emission dominated case (e.g., small flames). It overpredicts radiative heat loss (emission minus absorption), because of neglecting absorption. The PMC-LBL model gives the true radiative heat flux divergence. Therefore, the difference between the OT appoximation and PMC-LBL is the true self-absorption. A model is considered more accurate in resolving self-absorption if it is closer to PMC. A high-fidelity radiation modelling strategy, the combination of a spectral model and an RTE model, preserves the total emission and predicts most of the absorption. The model strategy must
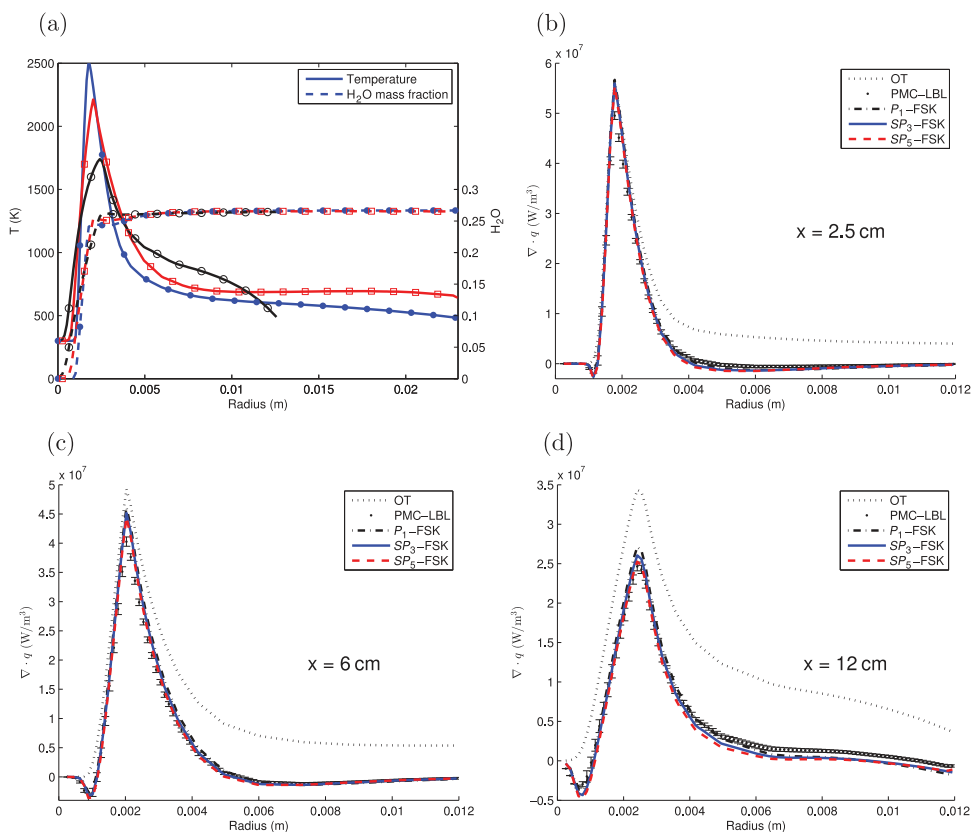
Figure 6. Radial profiles at 30 bar. (a) Radial profiles of temperature (solid line) and $H_2O$ mass fraction (dashed line) at $x = 2.5$ cm (line with bullets), 6 cm (line with squares) and 12 cm (line with circles). Radiative flux divergence ($\nabla \cdot q$) at $x = 2.5$ cm (b), 6 cm (c) and 12 cm (d) from the nozzle (colour online).

be applicable to a wide range of flame regimes, because the optical thickness is generally not known beforehand.

For the case of 1 bar, the profile at the downstream location 2.5 cm from the nozzle is shown (Figure 4). Consistent trends were found from 1 to 30 bar. For all pressures, the flame front has a higher temperature and corresponding higher emission near the nozzle (e.g., 2 cm from the nozzle). Absorption at the same location is small, as suggested by the overlapping predictions between the PMC and OT models, because this location is close to the inlet walls. Self-absorption becomes stronger inside the burner (e.g., 6 and 12 cm from the nozzle). In general, self-absorption becomes stronger as pressure increases. Strong self-absorption is observed in the recirculation zone (i.e., $r > 6$ mm) and is well predicted by all spherical harmonic models because of uniform temperature and species concentrations, whereas self-absorption in the flame front is more difficult to predict with the simple models. The differences between $P_1$, $SP_3$ and $SP_5$ predictions are small compared to their departures from the PMC-LBL model. For all pressures, the $P_1$, $SP_3$ and $SP_5$ models overpredict absorption especially along the flame front. $SP_3$ and $SP_5$ improve on $P_1$ predictions.
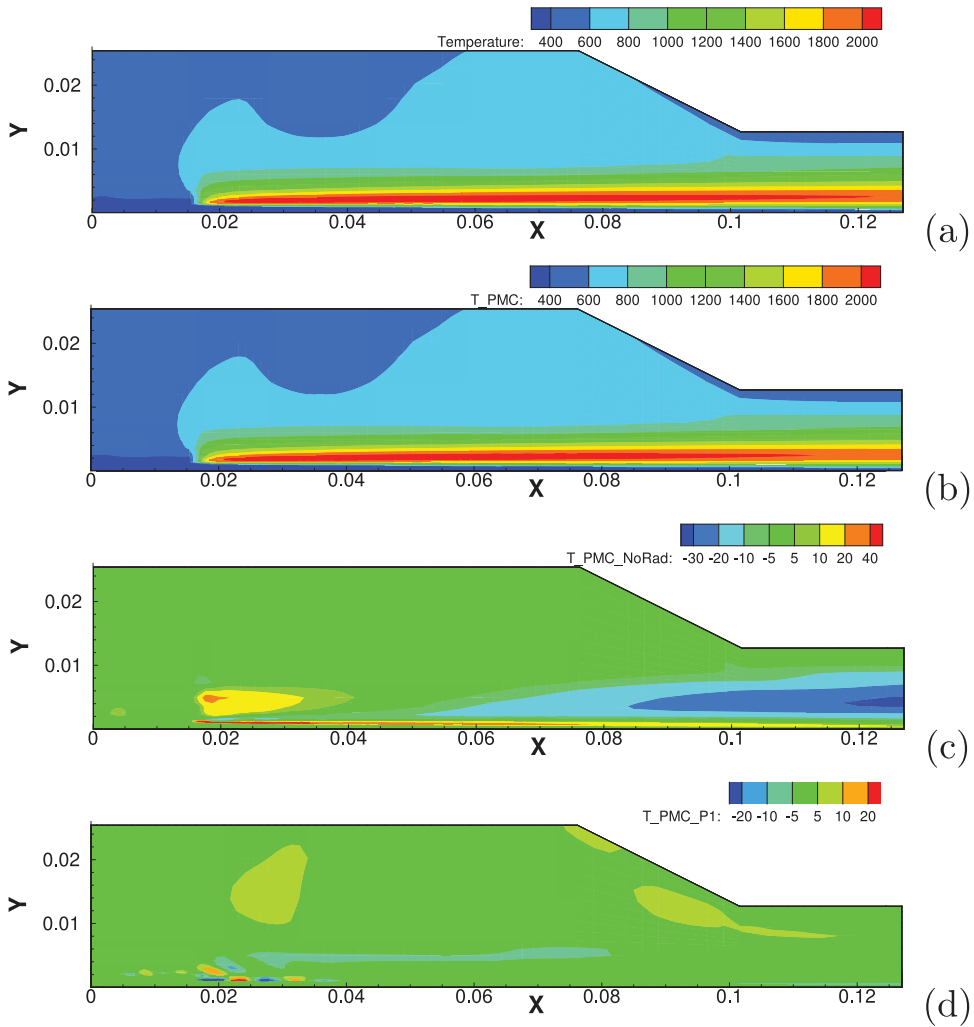
Figure 7.    Temperature profile at 1 bar. (a) Temperature without radiation; (b) temperature with radiation (PMC); (c) PMC − no radiation; (d) PMC-$P_1$.

### 3.3.    *Feedback calculations*

The flame structures at different pressures are illustrated by the temperature profiles. The flame front is recognized as the thin reaction zone with high temperature between fuel and oxidizer. Its evolution may be affected by radiation because of its high temperature and high concentration of radiatively participating species in combustion products. The leading edge of the flame front closest to the nozzle (the flame edge in the following text) is mostly affected by ignition chemistry. The temperature profiles are calculated with different radiation models with the remainder of the models fixed. The influence of the radiation model on the flame temperature is studied by calculating the difference in temperature predicted by different radiation models.

   The temperature profile calculated without radiation at 1 bar total pressure is shown in Figure 7(c). The flame is lifted from the burner because of the relatively fast jet velocity. The

temperature differences between with and without radiation are shown in Figures 7(c) using PMC with the LBL spectral model. The radiative heat transfer of water vapour formed in the flame front causes additional heat flux upon water vapour diffusion towards the central stream. Aside from changes to the flame front, little influence on the flame temperature is observed, because the optical thickness was found to be less than 0.03 based on the combustor diameter and the Planck-mean absorption coefficients.

The differences between different RTE solvers are found to be negligible because the optical thickness is small. For example, the temperature differences between $P_1$, $SP_3$ and $SP_5$ solvers using Full Spectrum $k$-distribution (FSK) methods are found to be mostly within 10 K (not shown). Random patterns of the temperature differences (Figure 7(d)) are due to numerical fluctuations in predicting the $k$-values at larger $g$-values, as they dominate the emission at the optically-thin limits.

When pressure is increased to 5 bar (Figure 8), the magnitude of the chemical source term increases with pressure faster than that of the radiative source term, which results in a thinner reaction zone. Faster reaction rates also cause the flame to be anchored closer to the nozzle. For higher-pressure cases, due to the larger density, the jet velocity is reduced to retain the Reynolds number and the residence time becomes correspondingly longer. The temperature decline due to radiation at downstream locations becomes more significant as a result of the longer residence time. The flame length is shortened by radiation, and radiation may cause a temperature decline of over 150 K at the combustor exit.

When radiation is considered (i.e., comparing temperature differences for calculations with and without radiation as shown in Figure 8(c)), the flame front temperature drops gradually at downstream locations due to emission. However, PMC predicts a smaller temperature drop than $P_1$ coupled with FSK (Figure 8(d)), as a result of overprediction of the radiative heat source by the $P_1$ solver. The overpredicted heat loss from the flame front is absorbed by the cooler water vapour in the recirculation zone, and this causes a corresponding temperature overprediction outside the flame front (i.e., the region of negative temperature difference between PMC and $P_1$). $P_1$, $SP_3$ and $SP_5$ solvers predict quantitatively similar temperature fields as indicated by the small differences in temperature predictions between these solvers (Figures 8(d)–8(f)). The outperformance of $P_1$, indicated by its closeness to PMC, leaves little margin for $SP_N$ solvers to improve.

Further increasing pressure from 5 to 10 bar (results not shown) will not bring the flame leading edge forward closer to the nozzle, because the flame edge position is now limited by the separation of fuel and nozzle, while at 1 bar the faster convection compared to thermal diffusion to the upstream lifts the flame. As the total pressure increases, the water vapour partial pressure increases, and this causes an increased emission at the flame edge. Because the flame edge is surrounded by the cold nozzle and unburnt gases, it absorbs little radiation. Therefore, PMC and FSK-$P_1$ give identical temperature drops and flame lift. Similar to the 5 bar case, $P_1$ overpredicts heat loss from the flame front, which causes a temperature rise adjacent to the flame front. However, because of the increased optical thickness and absorption, the affected region is much smaller than at 5 bar. The performance of $SP_3$ and $SP_5$ is quantitatively similar to that at 5 bar. Near the exit the temperature drop due to radiation increases to 200 K due to longer residence time.

Radiative effects are qualitatively similar but much stronger when the pressure is further increased to 30 bar because of the increased optical thickness and residence time, and are shown in Figure 9. Consistent temperature drops are predicted by PMC and $P_1$ along the flame front. Near the exit the temperature drop may be as large as 450 K. Similar to what has been found at 5 and 10 bar, $P_1$ overpredicts heat loss from the flame front and the temperature rise in the adjacent low temperature region, except that the size of the affected region becomes larger as pressure rises from 5 to 30 bar.
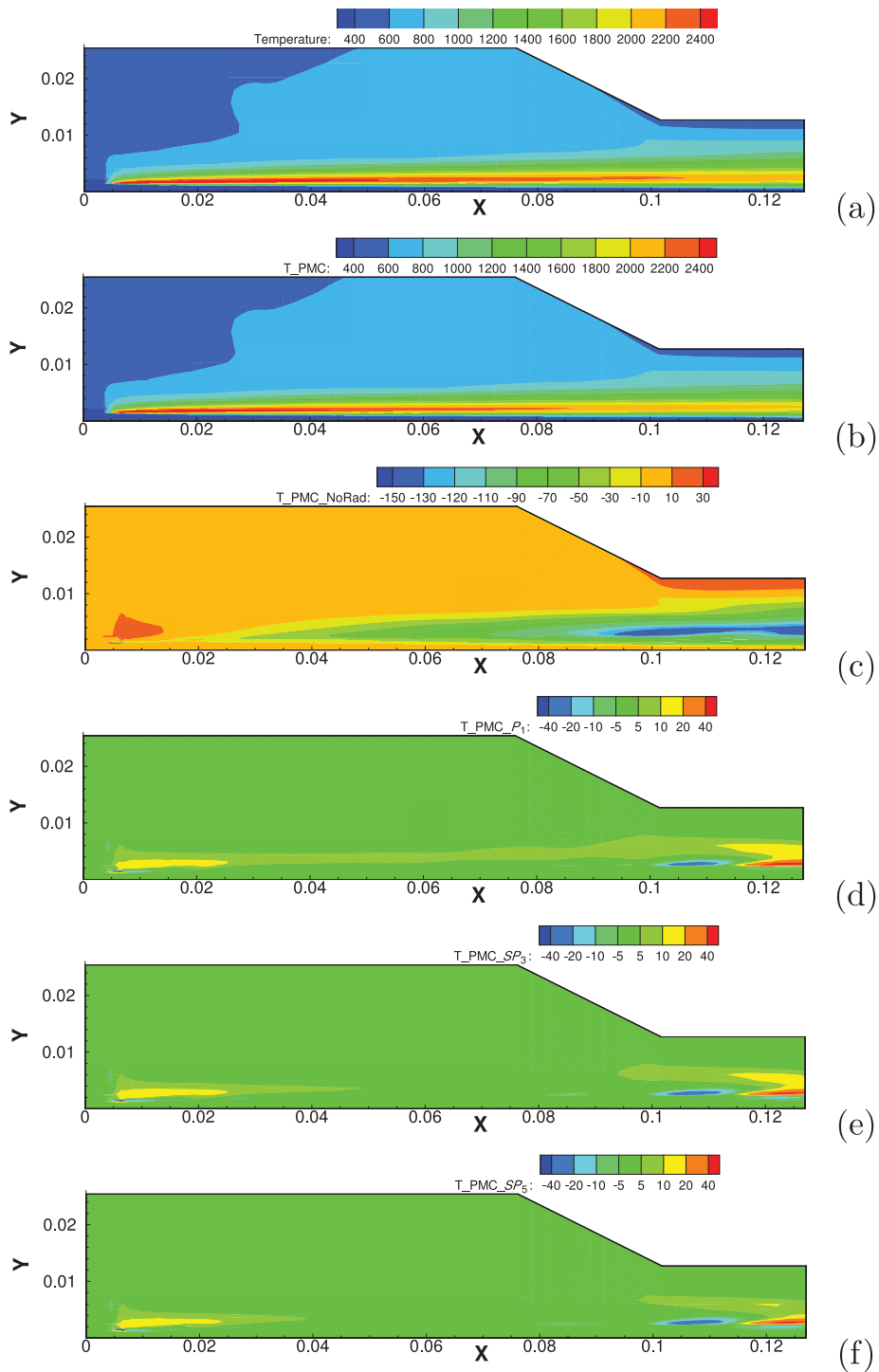
Figure 8.   Temperature profile at 5 bar. (a) Temperature without radiation; (b) temperature with radiation (PMC); (c) PMC − no radiation; (d) PMC-$P_1$; (e) PMC-$SP_3$; (f) PMC-$SP_5$.
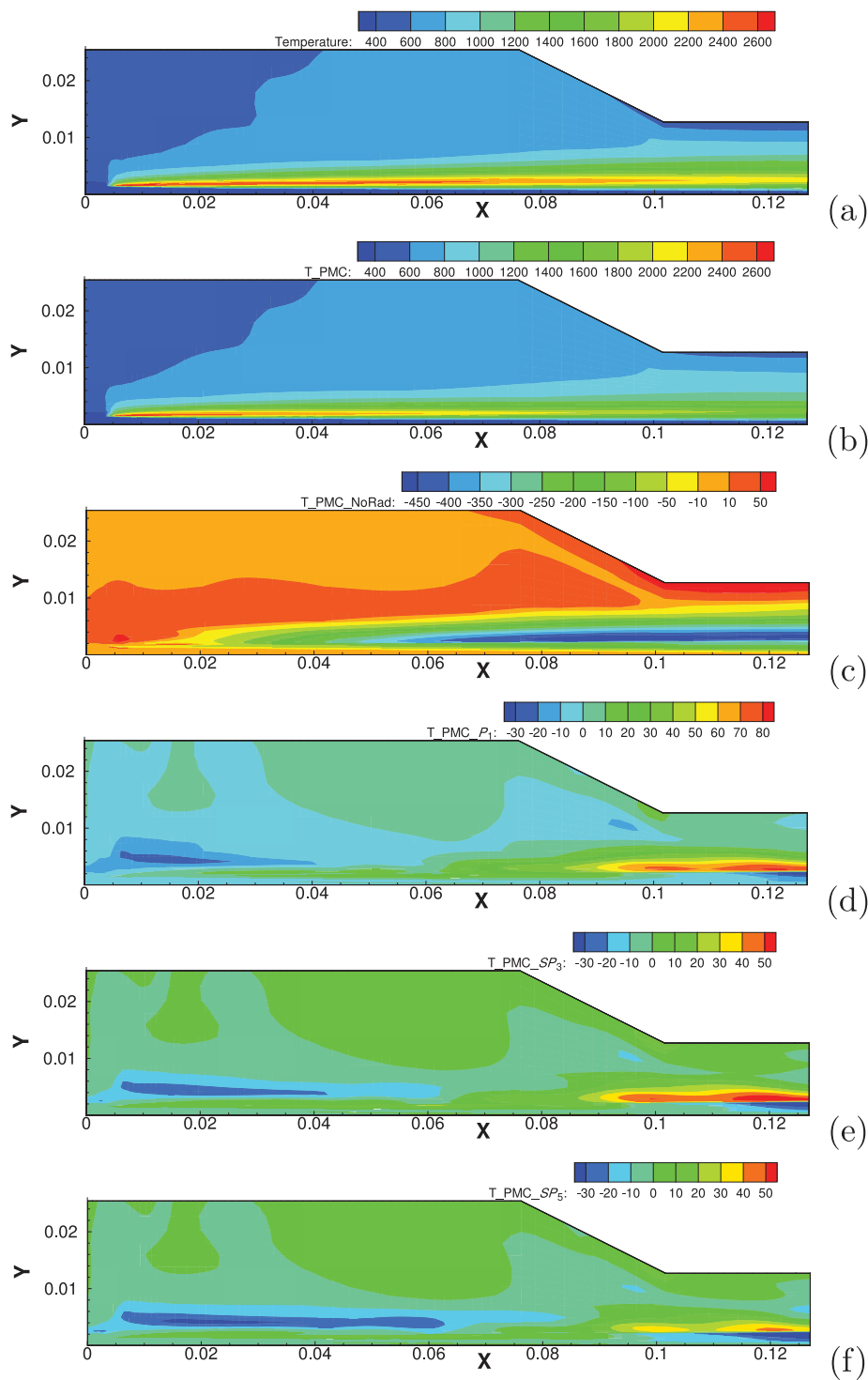
Figure 9.   Temperature profile at 30 bar. (a) Temperature without radiation; (b) temperature with radiation (PMC); (c) PMC − no radiation; (d) PMC-$P_1$; (e) PMC-$SP_3$; (f) PMC-$SP_5$.

All simulations were carried out on a cluster with four Intel(R) Xeon(R) X7460 CPUs. Each CPU has six cores. The computational cost of FSK-$P_1$, FSK-$SP_3$ and FSK-$SP_5$ is approximately 350 CPU hours each. Most of the computational time is spent on assembling $k$-distributions from the narrowband database . The additional cost of solving multiple equations in $SP_3$ and $SP_5$ is negligible compared to $k$-distribution calculations. The PMC-LBL time cost is approximately 600 CPU hours. Most of this time is due to Monte Carlo ray tracing and the calculation of emission wavelengths from the spectroscopic database.

The $k$-distribution methods, including the Full-Spectrum $k$-distribution (FSK) methods, are generic approaches to the spectral properties of non-grey radiatively participating media. The simplification of FSK comes from reduced RTE evaluations. A line-by-line model requires millions while the FSK needs only a few (we use eight in this study). The price is the computational cost to calculate $k$-distributions. FSK methods offer different model families with varying accuracy and efficiency. In a separate work [37], we reported comparisons on accuracy and efficiency between different FSK methods. The cheapest and least accurate (yet still vastly outperforming the grey) model takes 1 ms for a cell, while the most accurate and expensive model (employed here) achieves line-by-line accuracy. In this work, the fact that FSK is not taking much less time than PMC is for two reasons: (1) a time blending scheme for PMC is used in steady state flows which reduces PMC time cost by two orders of magnitude, which would not apply in transient problems; (2) the way we chose to evaluate the $k$-distributions takes the majority of time, because we aimed to demonstrate that full-spectrum $k$-distribution methods can achieve high accuracy. And with that accuracy we may further demonstrate the importance of radiation in high-pressure flames. Less accurate FSK assembling reduces the effort by about two orders of magnitude [37].

## 4. Conclusions

Radiative heat transfer is studied numerically for high-pressure laminar $H_2$–air jet diffusion flames, with pressure ranging from 1 to 30 bar. At atmospheric pressure the flame is optically thin, and little absorption is observed. The radiative emission causes little cooling down of temperature along the flame front and at the exit.

Radiative heat transfer effects become stronger as pressure increases due to both increased emission and longer residence time. Increased pressure also causes stronger self-absorption. As a result, the optically thin approximation, which ignores self-absorption, overpredicts the radiative heat loss. At higher pressure, the peak flame temperature is less affected by radiation because of faster chemical reactions. However, due to larger residence time, significant cooling at downstream locations is observed. As the optical thickness increases with pressure, the performances of three spherical harmonic RTE solvers ($P_1$, $SP_3$ and $SP_5$) start to deviate, but are still very close for the current case. In general, $P_1$ tends to predict a larger radiative heat loss than $SP_N$. It is found that $SP_N$ can only perform marginally better than $P_1$ on the calculation of radiative heat sources in this flame, because the $P_1$ model is adequate except at the very high pressure of 30 bar.

## Funding

## References

[1] A.H. Lefebvre and D.R. Ballal, *Gas Turbine Combustion: Alternative Fuels and Emissions*, 3rd ed., CRC Press, Hoboken, NJ, 2010.

[2] R. Viskanta and M.P. Mengüç, *Radiation heat transfer in combustion systems*, Progr. Energy Combust. Sci. 13 (1987), pp. 97–160.

[3] G.P. Sutton and O. Biblarz, *Rocket Propulsion Elements*, 8th ed., Wiley, Hoboken, NJ, 2011.

[4] M.P. Burke, M. Chaos, Y. Ju, F.L. Dryer, and S.J. Klippenstein, *Comprehensive $H_2/O_2$ kinetic model for high-pressure combustion*, Int. J. Chem. Kinetics 44 (2012), pp. 444–474.

[5] A. Wang, M.F. Modest, D.C. Haworth, and L. Wang, *Monte Carlo simulation of radiative heat transfer and turbulence interactions in methane/air jet flames*, J. Quant. Spectrosc. & Rad. Trans. 109 (2008), pp. 269–279.

[6] M.F. Modest, *Radiative Heat Transfer*, 3rd ed., Academic Press, New York, 2013.

[7] E.M. Gelbard, *Simplified spherical harmonics equations and their use in shielding problems*, Tech. Rep. WAPD-T-1182, Bettis Atomic Power Laboratory, Pittsburgh, PA, 1961.

[8] R.G. McClarren, *Theoretical aspects of the simplified $P_n$ equations*, Transp. Theory & Statist. Phys. 39 (2011), pp. 73–109.

[9] M.F. Modest and S. Lei, *Simplified spherical harmonics method for radiative heat transfer*, in *Proceedings of Eurotherm Seminar 95: Computational Thermal Radiation in Participating Media IV*, 18–20 April 2012, Nancy, France. J. Phys.: Conf. Ser. 369 (2012), Paper No. 012019. Available at http://dx.doi.org/10.1088/1742-6596/369/1/012019.

[10] A. Wang and M.F. Modest, *An adaptive emission model for Monte Carlo ray-tracing in participating media represented by statistical particle fields*, J. Quant. Spectrosc. & Rad. Trans. 104 (2007), pp. 288–296.

[11] L. Tessé, F. Dupoirieux, and J. Taine, *Monte Carlo modeling of radiative transfer in a turbulent sooty flame*, Int. J. Heat Mass Trans. 47 (2004), pp. 555–572.

[12] A. Wang and M.F. Modest, *Photon Monte Carlo simulation for radiative transfer in gaseous media represented by discrete particle fields*, ASME J. Heat Trans. 128 (2006), pp. 1041–1049.

[13] A.M. Feldick and M.F. Modest, *A spectrally accurate tightly-coupled 2-D axisymmetric photon Monte Carlo RTE solver for hypersonic entry flows*, ASME J. Heat Trans. 134 (2012), Paper No. 122701. Available at http://dx.doi.org/10.1115/1.4007069.

[14] X.L. Xia, D.P. Ren, and H.P. Tan, *A curve Monte Carlo method for radiative heat transfer in absorbing and scattering gradient-index medium*, Numer. Heat Trans. B 50 (2006), pp. 181–192.

[15] L. Soucasse, P. Rivière, and A. Soufiani, *Monte Carlo methods for radiative transfer in quasi-isothermal participating media*, J. Quant. Spectrosc. & Rad. Trans. (2013), pp. 34–42.

[16] A. Wang and M.F. Modest, *Spectral Monte Carlo models for nongray radiation analyses in inhomogeneous participating media*, Int. J. Heat Mass Trans. 50 (2007), pp. 3877–3889.

[17] T. Ozawa, M.F. Modest, and D.A. Levin, *Spectral module for photon Monte Carlo calculations in hypersonic nonequilibrium radiation*, ASME J. Heat Trans. 132 (2010), Paper No. 023406.

[18] A.M. Feldick and M.F. Modest, *Importance sampling in Monte Carlo ray tracing solutions applied to radiation in hypersonic entry flows*, in *Proceedings of the ASME/JSME 8th Thermal Engineering Joint Conference*, 13–17 March 2011, Honolulu, Hawaii, Paper No. AJTEC2011-44487. Available at http://dx.doi.org/10.1115/AJTEC2011-44487.

[19] T. Ren and M.F. Modest, *Hybrid wavenumber selection scheme for line-by-line photon Monte Carlo simulations in high-temperature gases*, ASME J. Heat Trans. 135 (2013), Paper No. 084501.

[20] J. Taine, *A line-by-line calculation of low-resolution radiative properties of $CO_2$–CO–transparent nonisothermal gases mixtures up to 3000 K*, J. Quant. Spectrosc. & Rad. Trans. 30 (1983), pp. 371–379.

[21] H. Zhang and M.F. Modest, *A multi-scale full-spectrum correlated-k distribution for radiative heat transfer in inhomogeneous gas mixtures*, J. Quant. Spectrosc. & Rad. Trans. 73 (2002), pp. 349–360.

[22] L. Wang and M.F. Modest, *Narrow-band based multi-scale full-spectrum k-distribution method for radiative transfer in inhomogeneous gas mixtures*, ASME J. Heat Trans. 127 (2005), pp. 740–748.

[23] M.F. Modest and R.J. Riazzi, *Assembly of full-spectrum k-distributions from a narrow-band database; effects of mixing gases, gases and nongray absorbing particles, and mixtures with nongray scatterers in nongray enclosures*, J. Quant. Spectrosc. & Rad. Trans. 90 (2005), pp. 169–189.

[24] V.V. Toro, A.V. Mokhov, H.B. Levinsky, and M.D. Smooke, *Combined experimental and computational study of laminar, axisymmetric hydrogen–air diffusion flames*, Proc. Combust. Inst. 30 (2005), pp. 485–492.

[25] T.S. Cheng, C.Y. Wu, C.P. Chen, Y.H. Li, Y.C. Chao, T. Yuan, and T.S. Leu, *Detailed measurement and assessment of laminar hydrogen jet diffusion flames*, Combust. Flame 146 (2006), pp. 268–282.

[26] L.S. Rothman, I.E. Gordon, R.J. Barber, H. Dothe, R.R. Gamache, A. Goldman, V.I. Perevalov, S.A. Tashkun, and J. Tennyson, *HITEMP, the high-temperature molecular spectroscopic database*, J. Quant. Spectr. & Rad. Trans. 111 (2010), pp. 2139–2150.

[27] R.J. Kee, G. Dixon-Lewis, J. Warnatz, M.E. Coltrin, and J.A. Miller, *A Fortran computer code package for the evaluation of gas-phase, multicomponent transport properties*, Tech. Rep. SAND86-8246, Sandia National Laboratory, 1986.

[28] P.D. Neufeld, A.R. Janzen, and A.R. Aziz, *Empirical equations to calculate 16 of the transport collision integrals $\omega^{(l, s)*}$ for the Lennard–Jones (12–6) potential*, J. Chem. Phys. 57 (1972), pp. 1100–1102.

[29] P.N. Brown, G.D. Byrne, and A.C. Hindmarsh, *Vode: A variable-coefficient ODE solver*, SIAM J. Sci. Statist. Comput. 10 (1989), pp. 1038–1051.

[30] A.C. Hindmarsh and R. Serban, *User documentation for cvode v. 2.6.0*, Center for Applied Scientific Computing, Lawrence Livermore National Laboratory, 2009.

[31] M.F. Modest, *Narrow-band and full-spectrum k-distributions for radiative heat transfer – correlated-k vs. scaling approximation*, J. Quant. Spectrosc. & Rad. Trans. 76 (2003), pp. 69–83.

[32] A. Wang and M.F. Modest, *High-accuracy, compact database of narrow-band k-distributions for water vapor and carbon dioxide*, J. Quant. Spectr. & Rad. Trans. 93 (2005), pp. 245–261.

[33] D.H.D. West, *Updating mean and variance estimates: An improved method*, Commun. ACM 22 (1979), pp. 532–535.

[34] D. Bissel, *Statistical Methods for SPC and TQM*, Chapman and Hall, New York, 1994.

[35] OpenFOAM® website, http://www.opencfd.co.uk/openfoam/.

[36] R.S. Barlow and J.H. Frank, *Effects of turbulence on species mass fractions in methane/air jet flames*, Proc. Combust. Inst. 27 (1998), pp. 1087–1095.

[37] J. Cai, R. Marquez, and M. Modest, *Comparisons of radiative heat transfer calculations in a jet diffusion flame using spherical harmonics and k-distributions*, J. Heat Trans. 136 (2014). Available at http://dx.doi.org/10.1115/1.4026169.